Chapter 10

Broadly Tunable CW Terahertz Sources Using Intrinsic Josephson Junction Stacks in High-Temperature Superconductors

Manabu Tsujimoto, Takanari Kashiwagi,
Hidetoshi Minami and Kazuo Kadowaki

Additional information is available at the end of the chapter

http://dx.doi.org/Chapter DOI: 10.5772/67087

Abstract

Electromagnetic waves in the 0.3–3.0 THz frequency range are considered to have great potential in research and industry; thus, compact, solid-state and continuous-wave (CW) terahertz sources have been developed throughout the vast field of science and technology. Since the first demonstration of terahertz emission from intrinsic Josephson junctions (IJJs) in the high-temperature (high-T_c) superconductor $Bi_2Sr_2CaCu_2O_{8+\delta}$, terahertz generation utilizing stacks of IJJs has become a major topic of research, both experimentally and theoretically. In this chapter, we describe recent progress on the development of high-T_c superconducting terahertz sources. We demonstrate that these superconducting terahertz sources emit continuous terahertz radiation and generate power in the microwatt range at broadly tunable frequencies in the range of 0.5–2.4 THz. The solid-state source is extremely small in size and its output power is sufficiently stable during operation. In addition, we also established a transmission imaging system using high-T_c sources to promote effective use in various applications.

Keywords: CW terahertz source, high-temperature superconductor, intrinsic Josephson effect

1. Introduction

The intrinsic Josephson effect as a tunneling of cooper pairs between adjacent CuO_2 planes inside highly anisotropic high-temperature (high-T_c) cuprate superconductors has attracted

much experimental and theoretical attention since its experimental observation in 1992 by Kleiner et al. [1]. They observed the characteristic quasiparticle current-voltage branches corresponding to the individual switching of intrinsic Josephson junctions (IJJs) in single crystalline $Bi_2Sr_2CaCu_2O_{8+\delta}$ (Bi-2212), which consists of an atomic-scale stack of superconducting CuO_2 layers in between insulating Bi_2O_2 layers. **Figure 1(a)** shows the crystal structure of Bi-2212 and scheme of the IJJ. This experimental verification had a considerable influence on the concept of high-T_c superconductivity because it essentially ensures inhomogeneity of the superconducting order parameters. This rather surprising consequence naturally leads one to the new material concept of high-T_c superconductors as stacks of superconductor-insulator-superconductor devices. Some reviews of the phenomenon and the present status of research regarding the theoretical understanding have already been published [2]. In 1962, Josephson predicted that the tunneling current of cooper pairs through weakly coupled superconductors can be expressed as $J = J_c \sin(\varphi_2 - \varphi_1)$, where J_c is the critical current density and $(\varphi_2 - \varphi_1)$ is the phase difference of the wave functions in two superconductors [3]. When the current reaches J_c, a chemical potential difference $\mu_2 - \mu_1 = 2\text{eV}$ appears between two superconductors. The phase difference alters with time by $\varphi_2 - \varphi_1 = -(2\text{eV})t/\hbar$. Hence, an AC Josephson current, $J = J_c \sin(\omega_J t + \varphi_0)$, can be produced at the Josephson frequency

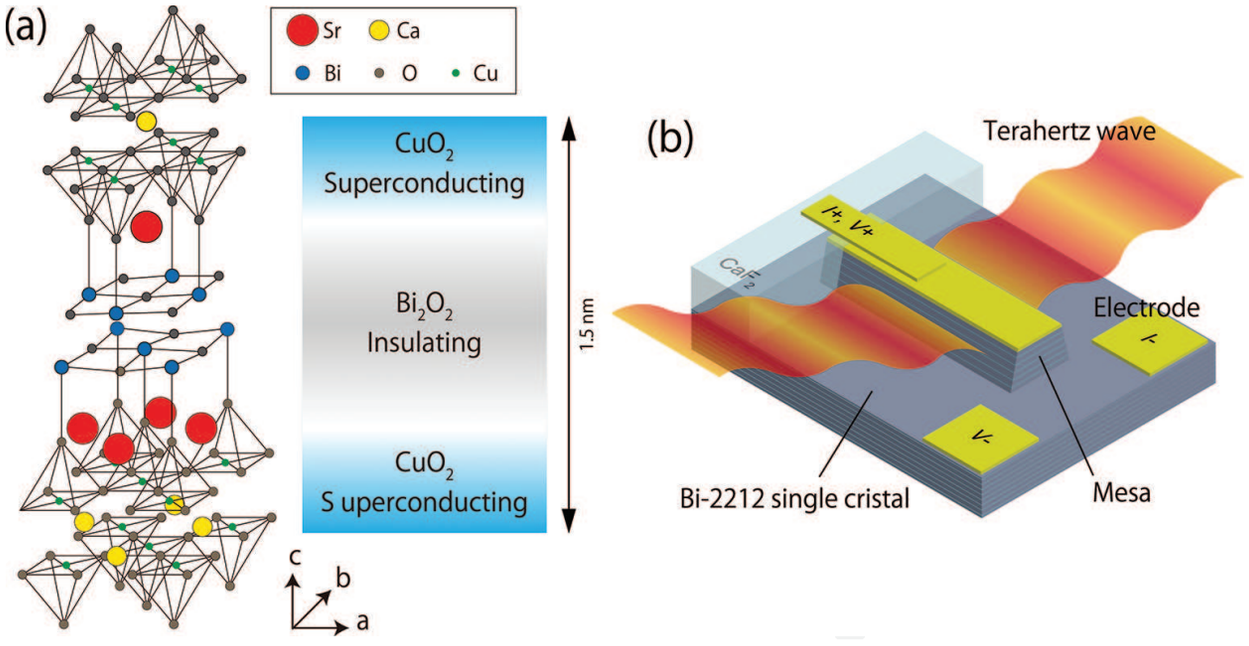

Figure 1. (a) Crystal structure of $Bi_2Sr_2CaCu_2O_{8+\delta}$ (Bi-2212) and scheme of the intrinsic Josephson junction. (b) Schematic view of the mesa-type high-T_c superconducting terahertz source.

$$f_J = \frac{\omega_J}{2\pi} = \frac{2e}{h}\text{V}. \tag{1}$$

As this universal relation is determined only by fundamental physical constants, the Josephson junction can act as a perfect DC/AC convertor: for example, application of 1 mV corresponds

http://dx.doi.org/Chapter DOI: 10.5772/67087

exactly to the generation of electromagnetic oscillation at 0.483 THz. A recent highlight was the development of flux-flow oscillators based on high-quality Josephson junctions [4]. The maximum electromagnetic radiation power generated typically ranges from several nanowatts to a few microwatts [5, 6], whereas the frequency tunability is strictly limited by the superconducting gap energy, which is typically 750 GHz for a niobium-based junction. The use of discrete arrays of Josephson junctions enables the emitted power, the linewidth and the impedance to be optimized by adjusting the topology of the circuit. Nevertheless, the maximum power is insufficient to permit Josephson junctions to be used as practical high-frequency sources. The reasons for this include poor impedance matching, microwave losses and significant power generation at higher harmonics. The voltage fluctuation causes a broadening of the spectral linewidth; for example, a typical linewidth of 160 MHz has been obtained [7]. However, a linewidth below 1 MHz is required to use Josephson junctions as local oscillators of a subTHz frequency band receiver.

In 1986, high-T_c superconductivity was discovered by Bednorz and Müller in the Ba-La-Cu-O system [8]. Subsequently, Maeda et al. found a new phase of Bi-2212, which is the representative compound in a series of Bi-based cuprate superconductors $Bi_2Sr_2Ca_{n-1}Cu_nO_y$ ($n = 1, 2, 3, \cdots$), exhibiting relatively high-T_c [9]; i.e., the T_c of $Bi_2Sr_2Ca_2Cu_3O_{10+\delta}$ with $n = 3$ exceeded 100 K. In a subsequent study, T_c records were achieved with Tl- and Hg-based cuprates of 125 K [10] and 135 K [11]. The reason why so many studies have been concentrating on the Bi-2212 phase is that large and high-quality single crystals of this material are easily grown by the floating zone method [12]. The cleavable crystal enables us to obtain a clear crystal surface, which is indispensable for studying the material properties. Accordingly, a number of interesting phenomena have been observed and discussed in the Bi-2212 system. For example, clear experimental evidence for the melting of the classic Abrikosov vortex lattice in a wide temperature range below T_c [13] was obtained as a consequence of a number of experimental and theoretical studies.

In 2007, Ozyuzer et al. [14] published the first report on the intense, continuous and coherent terahertz electromagnetic wave radiation from the IJJs in Bi-2212. **Figure 1(b)** shows a schematic view of the mesa-type IJJ terahertz source. Since this discovery, a great deal of interest has been drawn not only to the physical mechanism of the radiation but also to the possible variety of applications in the vast field of science and technology. In this chapter, the authors describe a study on the fundamental mechanism of terahertz radiation from the high-T_c superconductor Bi-2212 and recent developments in potential applications. Although a considerable number of theoretical studies have been conducted to understand the mechanism of terahertz radiation, our focus remains on the experimental work because of space limitations.

2. Experimental

2.1. Sample preparation

Single crystals of Bi-2212 were prepared by a traveling solvent floating zone (TS-FZ) technique [12]. This technique is appropriate for growing incongruent melting materials including

high-T_c cuprate superconductors. The TS-FZ technique has some remarkable advantages in comparison with other conventional techniques such as the flux method. For instance, the TS-FZ technique enables us to obtain high-purity single crystals because there is no need to use a container or crucible. In addition, the TS-FZ technique enables us to overcome the problem associated with the uncontrollable doping process of cationic elements, which is a key ingredient required for high-T_c superconductivity. Single crystals of Bi-2212 were grown in air at a growth rate of 0.5–1.0 mm/h using an infrared convergence-type floating zone furnace [15]. A molten zone forming between the crystal and the feed rod was placed at the center of the ellipsoidal mirrors. Counter-rotation of both the feed rod and crystal was used to achieve homogeneous heating of the zone and especially to promote mixing. The single crystal then grows as the feed rod and the crystal moves down simultaneously. An as-grown Bi-2212 single crystal rod can be easily cleaved into thin slabs using a knife and Scotch tape. In this chapter, as-grown crystals were annealed at 650°C for 24 hours in argon gas mixed with 0.1% oxygen in order to obtain slightly underdoped crystals. The temperature dependence of the *c*-axis resistance shows behavior typical of slightly underdoped Bi-2212, as shown in the inset of **Figure 3(a)**.

Bi-2212 mesa samples were fabricated either by the focused ion beam (FIB) milling technique or photolithography technique. A piece of cleaved Bi-2212 crystal with the dimensions 110.01 mm^3 was glued onto a sapphire substrate and silver and gold thin layers were evaporated onto it. In this study, the author attempted to fabricate three different types of mesa: *terrace-type*, *groove-type* and *stand-alone-type* mesas, as presented in **Figure 2(a)–(c)**, respectively. The *terrace-type* mesa was milled by using conventional photolithography and the argon ion milling technique. The *groove-type* mesa was fabricated by patterning a 10-μm wide groove around the mesa by FIB milling. The *stand-alone-type* mesa was made by depositing a narrow gold strip on a single crystal, followed by argon ion milling and cleavage from the milled substrate. Then, the mesa was attached to a thin gold layer covering the sapphire substrate. Thin gold wire electrodes were fixed onto the top surface of these mesas and the substrate by silver paste. In this study, one rectangular *terrace-type* mesa, one rectangular *stand-alone-type* mesa and *groove-type* mesas with three different geometrical shapes (rectangle, square and disk) were fabricated. The sample dimensions and profile curves were measured using atomic force microscopy (AFM). The obtained cross-sectional profile is considerably slanted and rounded at the edges, resulting in an approximately trapezoidal shape. Typically, the cross section of the upper section is approximately 10% smaller than that of the lower section. The total number of embedded junctions is estimated from the mesa height d.

2.2. Measurement setup

The current-voltage characteristics (IVCs) were measured with the conventional electrical circuit for a resistance measurement, as shown in **Figure 2(e)**. The load resistance R_{LO}, the standard resistor $R_S = 10\ \Omega$ and the mesa sample are connected in series to the function generator. The current I is obtained from the voltage drop at R_S. The mesa voltage V is measured directly using a DC differential amplifier. To measure the multiple IVC branches, we use the constant voltage source instead of the function generator. The load resistance R_{LO} is typically set to 100 Ω.

http://dx.doi.org/Chapter DOI: 10.5772/67087

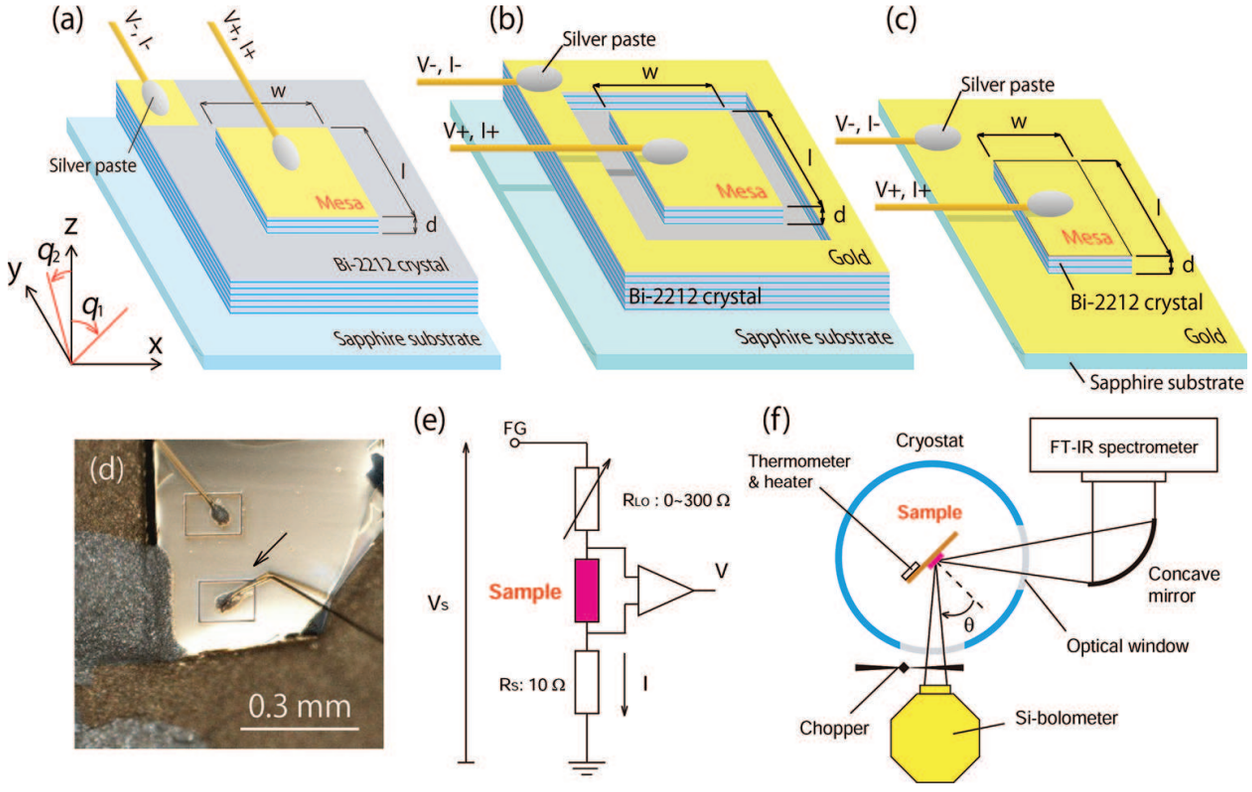

Figure 2. Schematic views of (a) terrace-type, (b) groove-type and (c) stand-alone-type mesa samples. (d) Optical microscopy image of the groove-type mesa sample. (e) Electrical circuit diagram for measuring IVCs. (f) Optical system for detecting the terahertz emission and measuring the emission frequencies.

Figure 2(f) shows an optical system for detecting the terahertz waves emitted from the sample. The output intensity is monitored during the bias scan using a Si bolometer. A He-flow type cryostat with two optical polyethylene windows was used for cooling the sample. The sample was mounted on a cold finger. The bath temperature T_b was monitored using a RhFe thermometer attached close to the cold finger. The detection angle θ can be adjusted by rotating the sample holder. The optical chopper was used to modulate the emitted terahertz wave at 80 Hz for the lock-in detection. We used a Fourier transform infrared (FT-IR) spectrometer to measure the emission frequencies.

3. Geometrical cavity resonance

The IVCs and terahertz-emission intensity for disk mesa D3 (*groove-type*, radius $a = 61.5$–65.0 μm and $d = 1.6$ μm) at $T_b = 25.0$ K are displayed in **Figure 3(a)** in black and red, respectively. In **Figure 3(b)**, the emission region is presented at an expanded scale. The most intense emission occurs on the return branch of the outermost IVC curve, where all stacking IJJs are in the resistive state. In most cases, the radiation is observed in a narrow I–V range; for example, $V = 0.96$–0.98 V and $I = 10.8$ mA for sample D3. As the bias current is decreased, emission suddenly ceases due to a jump to an internal IVC branch. It is interesting to note that emission usually occurs within a sample-dependent range of the base temperature of the mesa.

For example, mesa D3 emits between 10 and 50 K. During the emission, since a DC of I~11 mA is supplied to mesa D3, it is inevitably heated at 11 mW power. This huge heating power density cannot be removed quickly enough from the mesa to maintain equilibrium, resulting in a considerable increase of the mesa temperature [16]. The local heating may induce a chaotic nonequilibrium state and may adversely affect the emission of terahertz radiation.

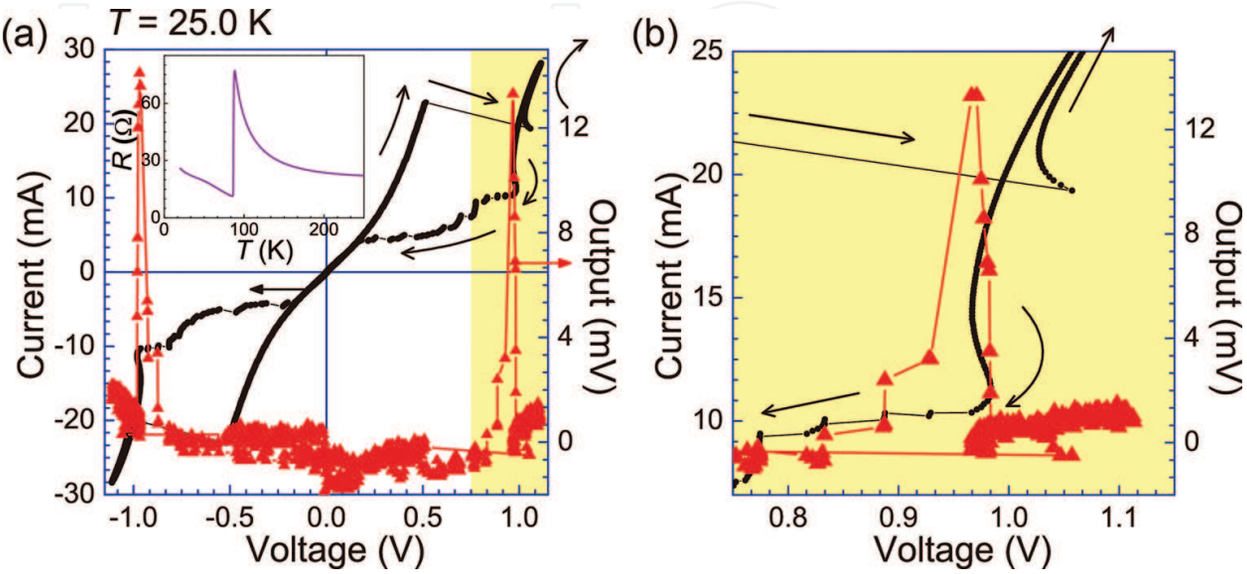

Figure 3. (a) IVCs (black, scale on the left) and output intensity detected using the Si bolometer (red, scale on the right) for disk mesa D3 at $T_b = 25.0$ K. (b) Details of the shaded high-bias regime in **Figure 3(a)** where the emissions are observed.

Figure 4(a) shows the far-infrared spectra of the terahertz radiation from three disk mesas with different radii: D1 ($a = 33.9$–38.9 μm), D1 ($a = 48.9$–51.5 μm) and D1 ($a = 61.5$–65.0 μm). The emission frequencies increase with decreasing radius, thereby indicating the geometrical cavity resonance effect. In **Figure 4(c)**, the emission frequency f is plotted as a function of $1/2a$. The dashed line represents the calculated cavity resonance frequency

$$f_{11}^{c} = \frac{\chi_{11} c_0}{2\pi n a}, \tag{2}$$

where $\chi_{11} = 1.841$ for the TM(1, 1) mode [17]. The emission frequency f is clearly proportional to $1/2a$. The data were fitted with $n = 4.2$, which is in good agreement with previous results [18]. Note that this n value is about 50% larger than that obtained from infrared spectroscopy [19]. In addition, for each disk mesa, the second harmonic at $2f$ is clearly visible and these frequencies are distinguishable from those of the nearest higher cavity modes [20].

The resonance frequencies of the TM(m, p) modes for a rectangular cavity of width w and length ℓ are in the form [21]:

$$f_{mp}^{c} = \frac{c_0}{2n}\sqrt{\left(\frac{m}{w}\right)^2 + \left(\frac{p}{\ell}\right)^2}. \tag{3}$$

It is very curious that the TM(0.1) mode for rectangular mesas has never been observed in previous experiments. Since the mesa is considerably heated by the DC current, the

http://dx.doi.org/Chapter DOI: 10.5772/67087

inhomogeneous temperature distribution inside the mesa prevents the formation of standing electromagnetic waves, particularly along the longer rectangular dimension. However, such hot spots with T even exceeding T_c, as observed by Wang et al. [22], do not seem to be a problem in our experiments, since the fundamental frequencies of disk mesas excellently obey the linear relationship of the cavity resonance frequency with the inverse of a. The discrepancies in relatively long rectangular mesas with $w \ll \ell = 300$–400 μm may have a different origin. This was verified by the fabrication of rectangular mesas with different ℓ/w ratios. **Figure 4(b)** shows the observed frequencies for rectangular mesas as a function of $1/w$. The dashed lines represent the cavity resonance frequencies for the TM(1,0) modes. It is obvious that the frequency obeys the TM(1,0) cavity resonance mode very well, definitely not the TM(0,1) resonance mode.

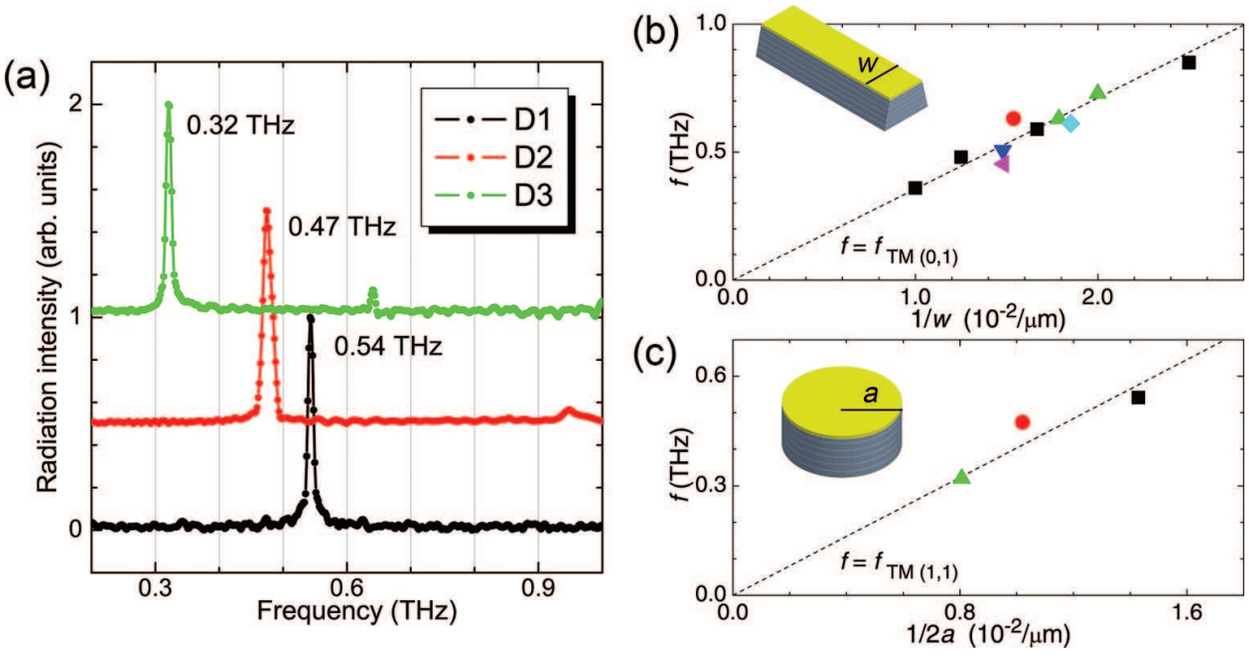

Figure 4. (a) Radiation spectra measured using a FT-IR spectrometer for three disk mesas. Observed frequencies f vs. $1/w$ for rectangular mesas (b) and $1/2a$ for disk mesas (c). The dashed lines represent the cavity resonance frequencies for TM (0,1) for the rectangular mesa and TM(1.1) for the disk mesa.

4. Anisotropic spatial emission patterns

The basic antenna theory excellently explains the spatial emission patterns of electromagnetic waves from the conventional antenna element, which consists of a normal metal, the dielectric material, etc., by solving Maxwell's equations for the electromagnetic fields. These electromagnetic waves originate from either an electric current flowing through the conducting surface or an electron charge orderly distributed within the element. Hence, measuring spatial emission patterns from the emitting device enables us to investigate both the internal electromagnetic fields and the surface current distribution. In the case of the IJJ terahertz source, the situation must be substantially different from the conventional antenna

element due to its superconducting characteristics. The excitation mode inside the disk mesa was investigated by measuring the angular dependence of the radiation intensity $I(\theta)$, where θ is the variable detection angle defined in **Figure 2(f)**.

Figure 5(a) shows $I(\theta)$ for disk mesa D3 in an arbitrarily fixed plane. The shadowing effect of the radiation from the superconducting Bi-2212 crystal wall outside the groove is expected to be negligibly small in the first approximation. In **Figure 5(a)**, the following characteristic features are noted: first, $I(\theta)$ is strongly anisotropic, having a maximum around $\theta = \theta_{max} = 20$–$35°$ from the top ($\theta = 0°$), where a local minimum occurs with the intensity ratio $I(20)/I(0)$~1.5–2.0—. This shallow minimum feature is almost the same as for rectangular mesas as discussed later, although θ_{max} is somewhat less than the corresponding rectangular mesa value. Second, $I(\theta)$ rapidly diminishes as θ approaches –90°. $I_{cav}(\theta)$ is calculated by assuming the TM(1,1) cavity mode alone which is shown as the black dashed curve in **Figure 5(a)** [20]. Clearly, the calculated $I_{cav}(\theta)$ does not fit the experimental data, especially near to $\theta = 0$, where $I_{cav}(\theta)$ is a maximum [20]. This disagreement can be removed by introducing the superposition of the radiation from the uniform AC Josephson current source with the same Josephson frequency, as described for rectangular mesas [18, 20]. Subsequent to similar calculations that were conducted by introducing the mixing parameter $\alpha = 1.44$ into the dual source model, where the mixing parameter corresponds to 41% of the radiation arising from the uniform AC Josephson current source, a more optimal fit is obtained for the experimental data as shown by the solid orange curve in **Figure 5(a)**. It is significant that the intensity from the uniform mode is comparable to that of the fundamental cavity mode, as in rectangular mesas [18]. Neither higher disk cavity excitation frequencies of the Bessel type nor subharmonics were observed in **Figure 4(a)**. This experimental evidence clarifies unambiguously that the terahertz radiation is mainly generated by the uniform mode of the AC Josephson current. However, it does not necessarily mean that the geometrical cavity resonance is not entirely unimportant for the determination of the actual radiation frequency values. An extended study of the spatial radiation patterns of the higher harmonics could provide additional supporting information for these conclusions.

The θ dependence of the radiation intensity for the rectangular mesa R3 (*terrace-type*, $w = 77.4$–4.5 μm, $\ell = 400$ μm and $d = 1.2$ μm) in the yz-plane $I(\theta_1)$ and in the xz-plane $I(\theta_2)$ are shown in **Figure 5(b)** and **(c)**, respectively, where $I(\theta_1)$ and $I(\theta_2)$ and the coordinates are defined in **Figure 2(a)**. As clearly seen that the observed emission has a considerably characteristic anisotropic pattern in comparison with the usual antenna elements. Typically in our results with other samples, the emission is usually stronger in the yz-plane than in the xz-plane, suggesting that the standing electromagnetic wave is certainly excited along the shorter side. The radiation intensities $I(\theta_1)$ in these figures are normalized at the maximum value obtained at $\theta_1 = \theta_2 = 0°$. As a result, the following characteristic features of spatial patterns are eventually obtained: first, $I(\theta_1)$ in the yz-plane has a maximum value, $I(\theta_1 = -30)/I(\theta_1 = 0)$~2, with a nearly symmetrical pattern. Second, $I(\theta_1)$ has a local minimum at the top, although it differs from sample to sample [18]. These commonly observed sample dependencies may arise from various differences in the properties among mesa samples, which are, for example, spatial inhomogeneities in the AC Josephson current due to a heating effect. Third, small but clear minor lobes are observed at $\theta_1 = \theta_2$~75° as shown in **Figure 5(b)** and **(c)**, whereas their integrated intensity appears to be only a few percentage less than the total. These lobes might

http://dx.doi.org/Chapter DOI: 10.5772/67087

be caused by the higher harmonics. The higher harmonics seems to hardly contribute to $I(\theta)$ because of the weakness as mentioned before. The standard antenna theory predicts that the radiation intensity $I(\theta)$ should reach a certain maximum value at the top of the mesa [23], where $\theta_1 = \theta_2 = 0°$ in the present system. However, our experimental results clearly show a different behavior from this prediction, in which the electromagnetic wave excitation is simply induced by the fundamental rectangular cavity mode. Here, if we assume a oscillating superconducting current spatially uniform in surface direction as well as in the case of disk mesa, $I(\theta)$ would rapidly diminish as θ approaches to 0° and would reach a maximum value at 90° resulting from the dipole radiation. Furthermore, in the actual case, the superconducting substrate of Bi-2212 and other obstructions in the optical path may also cause some complicated problems.

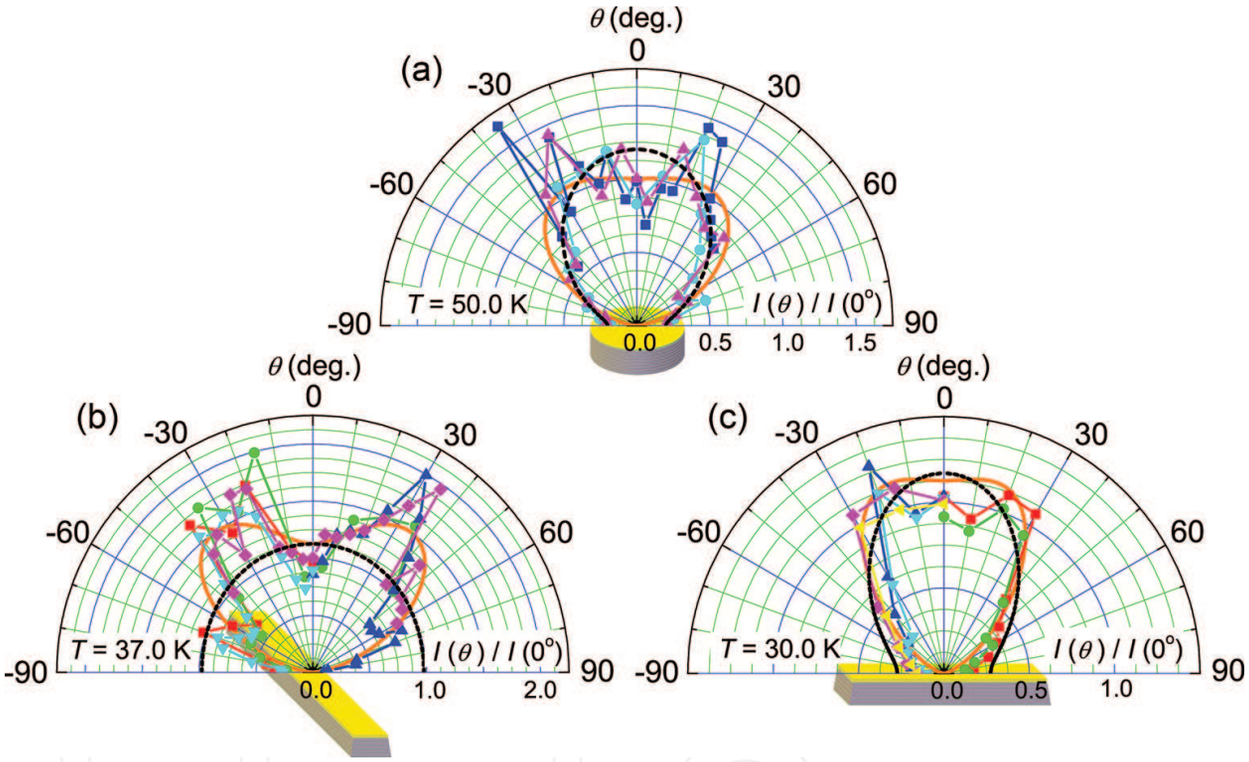

Figure 5. Polar plots of the radiation intensity $I(\theta)$ for (a) disk mesa and rectangular mesa in (b) *yz*-plane and (c) *xz*-plane. The solid and dashed lines are the best fits to the dual-source model and its cavity component, respectively.

5. Tunable radiation from internal current-voltage branches

Most workers considered the enhancement of the power of the output radiation by the excitation of an internal cavity mode to be such that the radiation from the AC Josephson current source alone was too weak to observe. However, recently, the contributions to the output power from the AC Josephson current source alone and that enhanced by resonance with an internal electromagnetic cavity source were found to be comparable in magnitude [18, 24]. Here, the authors show clear evidence that the mesas can emit radiation at many frequencies, without strong interaction with an internal cavity mode. More importantly, the resulting

radiation is tunable over a broad range of frequencies, allowing the possible construction of a powerful device that could fill the terahertz gap [25].

The authors found that electromagnetic emission also occurs at many points in the inner region of the multiply branched IVCs, where the number of the resistive IJJs $N = 1, 2, \cdots, N_{\max}$ is fixed but different for each branch. $N_{\max}$ is the number of IJJs in the stack estimated from the mesa height d. In **Figure 6(a)** and **(b)**, the radiation frequencies f are plotted as color-scaled symbols on the high-bias regions of the multiply branched IVC structures for R3 (*groove-type*, $w = 99.2$–102 μm, $\ell = 137$–140 μm and $d = 1.3$ μm) at $T_b = 35.0$ K and R2 (*stand-alone-type*, $w = 61.1$–63.7 μm, $\ell = 331$–333 μm and $d = 1.5$ μm) at $T_b = 52.5$ K, respectively. The insets show the full IVCs. All of the R1 curves in **Figure 6(a)** bend backwards with increasing current, indicative of Joule heating. However, R2 is less susceptible to heating effects and its IVCs in **Figure 6(b)** are monotonic. The radiation spectra were obtained at as many I–V bias points as possible. At some bias points, denoted by open diamonds, no emission was detected.

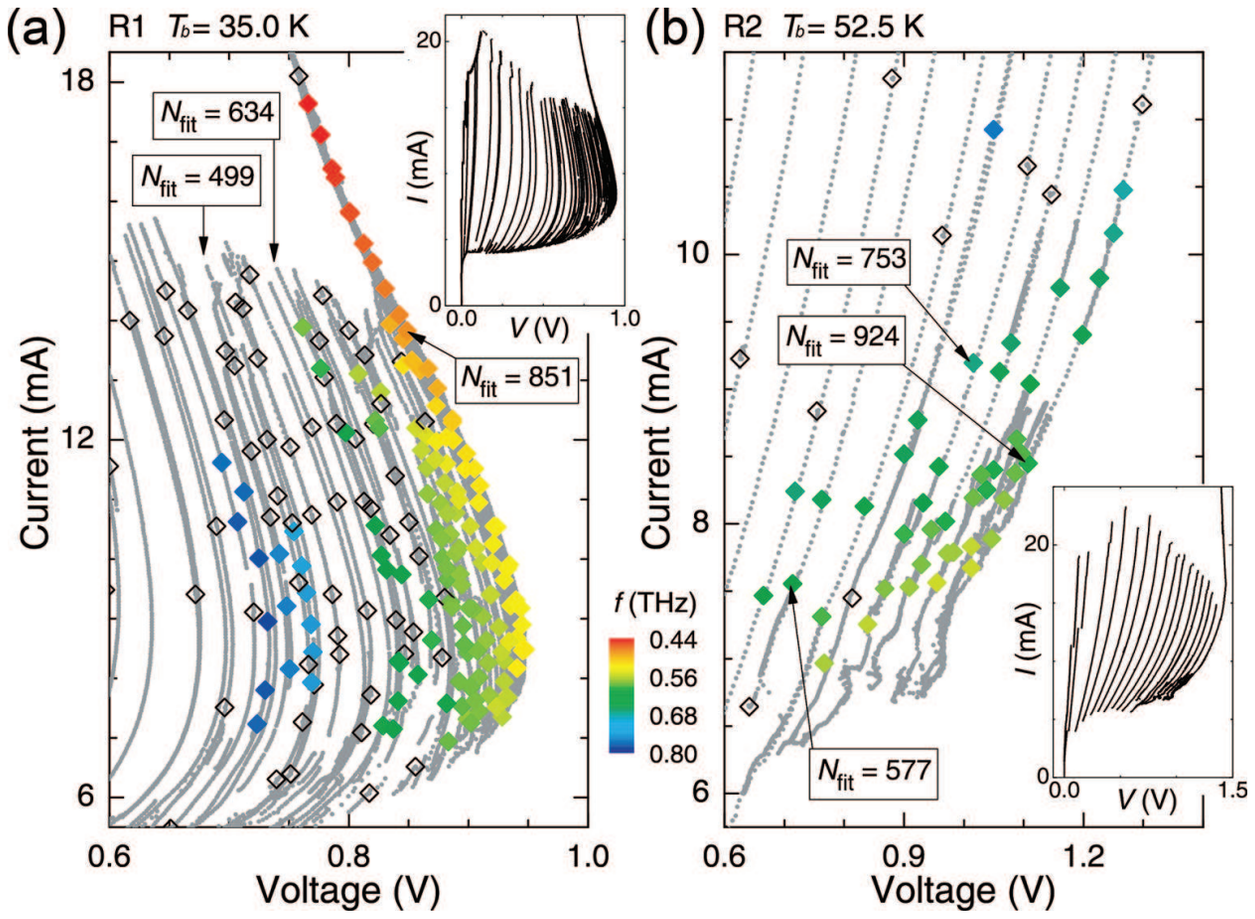

Figure 6. Emission at the color-coded frequencies was observed at the filled diamonds for R1 (a) and for R2 (b). No radiation was detected at the open diamonds. Arrows indicate the numbers of resistive junctions N_{fit} obtained from fits to the AC Josephson relation. The two insets show the full IVCs for each sample.

By repeated measurements of the emission from a particular IVC branch with constant N, the author confirmed that f satisfies the AC Josephson relation $f = f_J = (2e/h)V/N$. In **Figure 7(a)**, the emission data from the IVCs of R1 shown in **Figure 6(a)** was replotted in terms of $f(V)$, representing the data from each branch in terms of unique symbols and colors. By

http://dx.doi.org/Chapter DOI: 10.5772/67087

fitting the data for a particular branch to the AC Josephson relation with $N = N_{\text{fit}}$, the experimental best-fit value N_{fit} for each emitting branch was determined. Three examples each for R1, respectively, are indicated by the dashed lines in **Figure 7(a)** and the arrows in **Figure 6(a)**. In the inset in **Figure 7(a)**, the entire emission data from the respective inner branches are plotted as $f(V/N_{\text{fit}})$. For both R1 and R2, the AC Josephson relation $f = f_J = (2e/h)V/N_{\text{fit}}$ is very well obeyed. As **Figure 7(a)** clearly demonstrates that f is slightly tunable on each branch (indicated by a fixed symbol and color), in **Figure 7(b)** and **(c)**, we replotted the data from each respective R1 and R2 branch as $f(N_{\text{fit}})$. Although for both samples f is tunable as indicated by the vertical bars for each fixed branch number N_{fit}, R1 and R2 display rather different aspects of tunability. The overall tunability of the two samples is nearly the same, with R1 and R2, respectively, being tunable from 0.44 to 0.78 THz and from 0.43 to 0.76 THz, respectively. However, for R1, this range is primarily due to the f-dependence on the IVC branch number, whereas for R2, the tunability is greatest on a single branch.

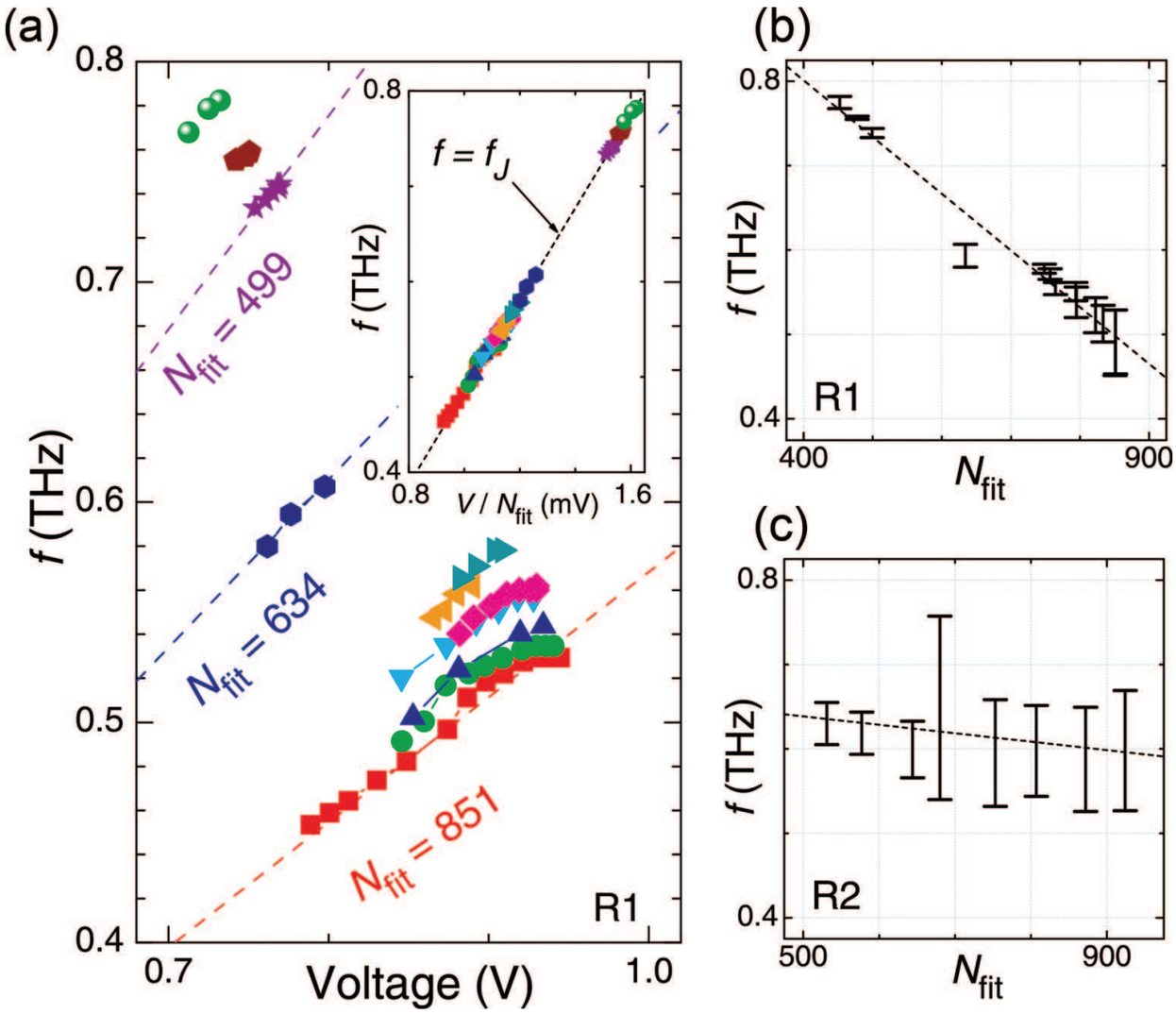

Figure 7. (a) Plots of $f(V)$ for 11 IVC branches for R1. The three dashed lines represent the theoretical fits to $f = f_J = (2e/h)V/N_{\text{fit}}$. The inset shows the plot of $f(V/N_{\text{fit}})$ for all R1 data with a $f = f_J$ line. Plots of $f(N_{\text{fit}})$ ranges for R1 (b) and R2 (c). The dashed curves serve to guide the eye.

6. Applications: terahertz imaging system

Radiation in the frequency range of 0.1–10 THz, known as terahertz waves, is known to be the most unique across the entire range of electromagnetic wavelengths, because of the unavailability of compact and convenient sources [25] of radiation of these wavelengths. In recent years, much effort has been made to overcome the above difficulty, particularly in the field of semiconductors and laser technologies. Resonant tunneling diodes [26], unitraveling-carrier photodiodes [27] and a quantum cascade laser [28] have been developed as useful terahertz sources. Recently, graphene and carbon nanotubes have also been reported as good candidates for terahertz wave generators [29, 30].

Because terahertz waves have the properties of being able to pass through various objects, such as plastics, paper, ceramics, semiconductors, liquids and proteins, similar to radio waves, they enable us to obtain images of various cm-by-cm wide substances [31], where the spatial resolution is actually determined by the wavelength of the terahertz wave, typically 1 mm. Since the radiation damage to these soft objects is known to be negligibly small in contrast to that inflicted by X-rays, in fact there is much demand for the nondestructive and noninvasive imaging technique in the field of the material inspection, medical diagnostics, security checks and environmental monitoring. Moreover, measuring the absorption spectrum in the terahertz region, where various molecular vibration modes of organic and high-molecular compounds dominate the electromagnetic wave absorption, one can identify the chemical substances both qualitatively and quantitatively. To realize these applications, compact, solid state and reliable source devices are strongly desired in spite of their technical difficulties.

Previous studies found that the present IJJ system can be used as a terahertz source device emitting continuous and microwatt power terahertz waves at tunable frequencies between 0.5 and 2.4 THz [32]. These device characteristics enable us to accumulate the data for an individual measurement point at high resolution in a few milliseconds or less. A solid-state IJJ device is extremely small in size and its output power is sufficiently stable during operation. We have attempted to demonstrate a terahertz imaging experiment using IJJ sources in order to promote the effective use of the present IJJ device for various practical applications.

The imaging system consists of a He-flow cryostat, two off-axis parabolic mirrors, a scan stage and a fast hot-electron (HE) bolometer as shown in **Figure 8(a)**. Two off-axis parabolic mirrors 1 and 2 with focal lengths of 152.4 and 220 mm and diameters of 75 mm are set to focus the terahertz waves on the sample. The imaged object is fixed on a 1-mm thick quartz plate and scanned in both the *X*-(horizontal) and *Z*-(vertical) directions using a biaxial scanner at a variable speed below 130 mm/s. The practical maximum speed should be 80 mm/s, which corresponds to a 5-ms time constant per data point when the measurement step is set to submillimeter levels. Although the IJJ emitting device can be modulated much faster above 500 kHz, in the present setup the maximum scan speed only depends on the minimum time constant of the lock-in amplifier. Nevertheless, the actual imaging has been performed at the speed of 32 mm/s in order to obtain sufficient data points. Before starting every scan, the optical path presented in **Figure 8(a)** is precisely adjusted by using the visible light from a photodiode attached to the source position as reference. A high-speed InSb HE bolometer

http://dx.doi.org/Chapter DOI: 10.5772/67087

placed directly behind the scan stage is used for measuring the output intensity of the terahertz waves passing through the sample. The IVCs of the IJJ device and the terahertz output intensity are simultaneously monitored using two oscilloscopes (OSCs). The photograph in the lower left part of **Figure 8(a)** shows the imaging system viewed from the top.

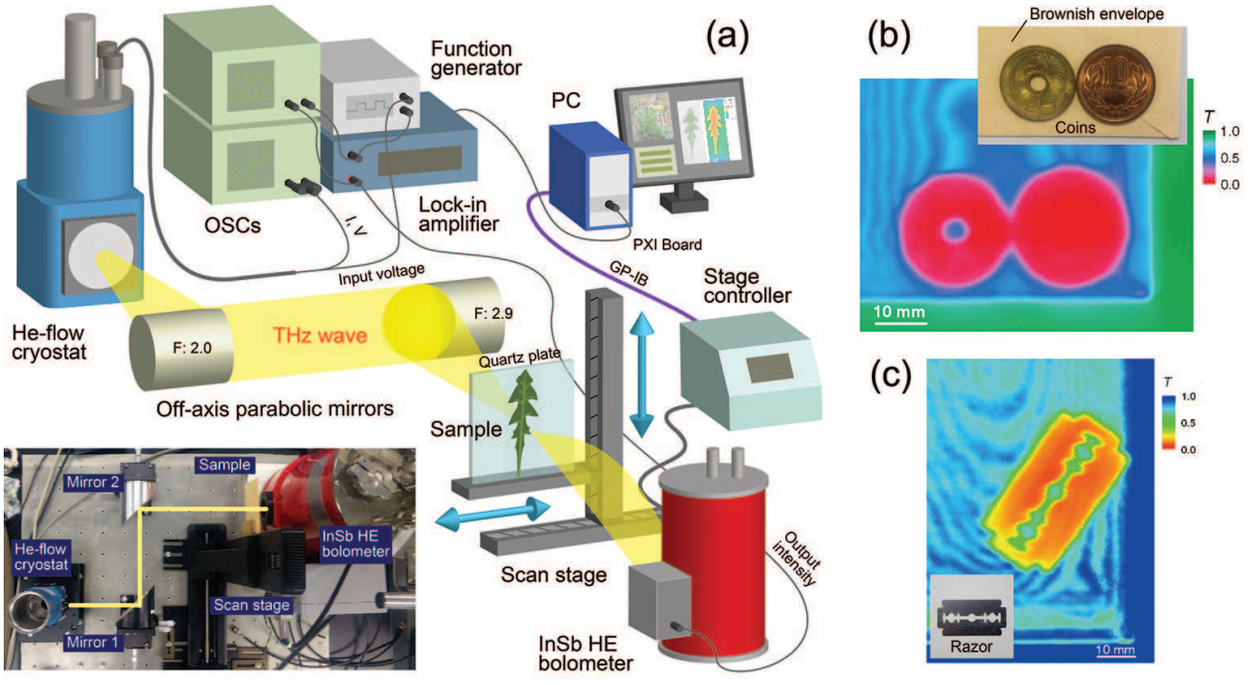

Figure 8. (a) Schematic diagram of the terahertz imaging system. The left lower photograph presents the actual system viewed from above. Terahertz images of 5-yen (left) and 10-yen (right) coins (b) and a razor blade (c) placed inside a brownish paper envelope. In these figures, the transmittance T is plotted in a color-coded scale. The photograph of each object is presented beside their terahertz image.

An imaging experiment was performed with the following procedure: first, pulse-modulated terahertz waves were generated from the IJJ source as follows: the DC source voltage is modulated by a low-amplitude square wave below 100 mV at 10 kHz and then applied to the device using the function generator. Maximum intensity is obtained by adjusting the offset level of the DC voltage and stabilized well to minimize power fluctuations by adjusting the amplitude of the square wave. The input current and the voltage were simultaneously monitored using an OSC (see **Figure 8(a)**). The imaging data are accumulated by simultaneous measurement of the sample position in the X- and Z-directions and the detected intensity. The intensity is acquired by an AD converter installed in a PXI bus system (National Instruments Co.) through the analog output channel of the lock-in amplifier. Some parameters such as scanning speed, measurement area and measurement step could be set by a homemade LabVIEW program. The obtained data are directly stored on the hard-disk drive and are simultaneously displayed on the PC screen in real time.

As test examples, the terahertz transmission images of two Japanese coins and a thin razor blade placed inside a brownish envelope presented in **Figure 8(b)** and **(c)**, respectively, were recorded. The photographs of these objects are presented beside their terahertz images. The

emission frequency was set to 0.54 THz. Note that the envelopes were attached to the scan stage without using a quartz plate. The screen size of the image in **Figure 8(b)** is 330250 pixels, which corresponds to a measurement step of 0.20.2 mm^2, whereas those of **Figure 8(c)** are 6080 pixels and 0.40.2 mm^2, which were appropriately set in terms of the required spatial resolution. It took at least 20 minutes to acquire each image. The observed image clearly reflects the transmittance T of pixels corresponding to the measurement step of 0.20.2 mm^2 of the terahertz wave through objects. The hole in the center of the 5-yen coin, which has a diameter of exactly 5 mm, is vividly shown in **Figure 8(b)** (left). The estimated spatial resolution of ~1 mm is comparable with the Rayleigh limit. Based on the results shown in **Figure 8(b)**, the calculated transmittance of one sheet of paper is 79% and it is clear that the coins are not transparent at all. It is interesting to note that several interference fringe-like patterns in the deeper blue area in **Figure 8(b)** and **(c)** are clearly observed. Assuming that terahertz waves with a wavelength of $\lambda = c_0/f = 0.56$ mm are reflected at the inner walls of the envelope and interfere with each other, the interference condition would be expressed as $2t_{\mathrm{m}} = (\lambda/2)2m$, where t_m is the interspace distance between the inner walls of the envelope and m is an integer. Hence, the distance between two neighboring fringes should be expressed as $t_{\mathrm{m+1}}-t_{\mathrm{m}} = \lambda/2 = 0.28$ mm. Since the thickness of the coin is 1.5 mm, at least $1.5/0.28\tilde{5}$–6 concentric fringes are expected to appear around the coins. This simple estimation agrees with the experimental result shown in **Figure 8(b)**. The interference effect is a unique property of monochromatic terahertz waves, which may be useful for versatile purposes in applications of interferometry and a wide variety of communications.

7. Summary

This chapter presents studies of terahertz electromagnetic wave emission from intrinsic Josephson junctions in the high-temperature superconductor $Bi_2Sr_2CaCu_2O_{8+\delta}$ (Bi-2212) and its device applications. This chapter started with the introduction of the Josephson effect and other basic formulations. Some historical developments concerning electromagnetic wave emission from conventional junctions and arrays were mentioned as a pioneering contribution to the present study. Sample preparation techniques and experimental setups were introduced. Photolithography, argon ion milling and focused ion beam milling were discussed as techniques that were used for the fabrication of *terrace-type*, *groove-type* and *stand-alone-type* mesa structures. The geometrical resonance conditions were investigated using several mesas with different geometrical shapes and sizes. The experimental results clearly demonstrate the validity of the cavity resonance model. The spatial radiation patterns were measured and analyzed for disk and rectangular mesas. As a result, significant anisotropic emission patterns depending on the mesa geometry were observed. These results can naturally be understood by introducing the mechanism that combines two radiation sources: the AC Josephson current and cavity mode excitation. The current-voltage characteristics of the internal branches, which were found to emit radiation across a broad frequency range, were examined to determine whether the excitation of an internal cavity mode was an essential feature of the coherent radiation. Hence, it was concluded that the primary source of the intense, coherent subTHz radiation is the AC Josephson current

http://dx.doi.org/Chapter DOI: 10.5772/67087

and that the internal electromagnetic cavity produced by the geometrical shape of the emitting mesa is at the best of minor importance. The final part of this chapter presents a demonstration of the terahertz imaging system using high-T_c superconducting terahertz sources. As text examples, terahertz images of coins and a razor blade placed inside a brownish paper envelope were presented. These images enable the interference fringes caused by the monochromatic terahertz waves to be clearly observed. These demonstrations strongly confirm that this imaging system would be useful in many practical applications, such as medical tissue diagnosis, food inspection, biological and biomedical imaging and environmental monitoring.

Several phenomena relating to terahertz radiation from high-T_c superconductors remain poorly understood. For instance, in some cases, two kinds of emission were found to be taking place in two current-voltage regions: stable emission near the fully resistive region and unstable emission in the retrapping region. Understanding a complicated situation, it requires a thorough investigation of the thermal properties of the system, such as the temperature distribution inside the mesa. In addition, it is not obvious whether there is an upper limit to the radiation intensity and even to the radiation frequency. The effect of a magnetic field on terahertz emission continues to remain unclear, although selected theoretical predictions regarding the enhancement of the radiation intensity have been published. Hence, further studies are undoubtedly needed in order to elucidate these fascinating phenomena.

Author details

Manabu Tsujimoto*, Takanari Kashiwagi, Hidetoshi Minami and Kazuo Kadowaki

*Address all correspondence to: tsujimoto@ims.tsukuba.ac.jp

Division of Materials Science, Faculty of Pure and Applied Sciences, University of Tsukuba, Tsukuba, Japan

References

[1] R. Kleiner, F. Steinmeyer, G. Kunkel and P. Müller, Phys. Rev. Lett. **68**, 2394 (1992).

[2] A. Yurgens, Supercond. Sci. Technol. **13**, R85 (2000).

[3] B. D. Josephson, Phys. Lett. **1**, 251 (1962).

[4] V. P. Koshelets, S. V. Shitov, L. V. Filippenko, A. M. Baryshev, W. Luinge, H. Golstein, H. van de Stadt, J.R. Gao and T. de Graauw, IEEE Trans. Appl. Supercond. **7**, 3589 (1997).

[5] A. V. Ustinov, S. V. Shitov, N. Iosad and H. Kohlstedt, IEEE Trans. Appl. Supercond. **7**, 3601 (1997).

[6] J. Mygind, V. P. Koshelets, A. V. Shchukin, S. V. Shitov and I. L. Lapytskaya, IEEE Trans. Appl. Supercond. **5**, 2951 (1995).

[7] A. K. Jain, K. K. Likharev, J. E. Lukens and J. E. Sauvageau, Phys. Rep. **109**, 309 (1984).

[8] J. G. Bednorz and K. A. Müller, Zeitschrift Für Phys. B Condens. Matter **64**, 189 (1986).

[9] H. Maeda, Y. Tanaka, M. Fukutomi and T. Asano, Jpn. J. Appl. Phys. **27**, L209 (1988).

[10] Z. Z. Sheng and A. M. Hermann, Nature **332**, 138 (1988).

[11] A. Schilling, M. Cantoni, J. D. Guo and H. R. Ott, Nature **363**, 56 (1993).

[12] M. J. V. Menken, A. J. M. Winkelman and A. A. Menovsky, J. Cryst. Growth **113**, 9 (1991).

[13] E. Zeldov, D. Majer, M. Konczykowski, V. B. Geshkenbein, V. M. Vinokur and H. Shtrikman, Nature **375**, 373 (1995).

[14] L. Ozyuzer, A. E. Koshelev, C. Kurter, N. Gopalsami, Q. Li, M. Tachiki, K. Kadowaki, T. Yamamoto, H. Minami, H. Yamaguchi, T. Tachiki, K. E. Gray, W.K. Kwok and U. Welp, Science **318**(80), 1291 (2007).

[15] T. Mochiku and K. Kadowaki, Phys. C Supercond. **235–240**, 523 (1994).

[16] A. Yurgens, Phys. Rev. B **83**, 184501 (2011).

[17] A. Derneryd, IEEE Trans. Antennas Propag. **27**, 660 (1979).

[18] K. Kadowaki, M. Tsujimoto, K. Yamaki, T. Yamamoto, T. Kashiwagi, H. Minami, M. Tachiki and R. A. Klemm, J. Phys. Soc. Japan **79**, 23703 (2010).

[19] S. Tajima, G. D. Gu, S. Miyamoto, A. Odagawa and N. Koshizuka, Phys. Rev. B **48**, 16164 (1993).

[20] R. A. Klemm and K. Kadowaki, J. Phys. Condens. Matter **22**, 375701 (2010).

[21] M. Tsujimoto, I. Kakeya, T. Kashiwagi, H. Minami and K. Kadowaki, Opt. Express **24**, 4591 (2016).

[22] H. B. Wang, S. Guénon, B. Gross, J. Yuan, Z. G. Jiang, Y. Y. Zhong, M. Grünzweig, A. Iishi, P. H. Wu, T. Hatano, D. Koelle and R. Kleiner, Phys. Rev. Lett. **105**, 57002 (2010).

[23] M. Leone, IEEE Trans. Electromagn. Compat. **45**, 486 (2003).

[24] M. Tsujimoto, K. Yamaki, K. Deguchi, T. Yamamoto, T. Kashiwagi, H. Minami, M. Tachiki, K. Kadowaki and R. A. Klemm, Phys. Rev. Lett. **105**, 37005 (2010).

[25] M. Tonouchi, Nat. Photonics **1**, 97 (2007).

[26] E. R. Brown, J. R. Söderström, C. D. Parker, L. J. Mahoney, K. M. Molvar and T. C. McGill, Appl. Phys. Lett. **58**, 2291 (1991).

[27] H. Ito, T. Furuta, F. Nakajima, K. Yoshino and T. Ishibashi, J. Light. Technol. **23**, 4016 (2005).

[28] J. Faist, F. Capasso, D. L. Sivco, C. Sirtori, A. L. Hutchinson and A. Y. Cho, Science. **264** (80), 553 (1994).

http://dx.doi.org/Chapter DOI: 10.5772/67087

[29] N. L. Rangel and J. M. Seminario, J. Phys. Chem. A **112**, 13699 (2008).

[30] O. V Kibis, M. Rosenau da Costa and M. E. Portnoi, Nano Lett. **7**, 3414 (2007).

[31] K. Kawase, Opt. Photonics News **15**, 34 (2004).

[32] T. Kashiwagi, K. Sakamoto, H. Kubo, Y. Shibano, T. Enomoto, T. Kitamura, K. Asanuma, T. Yasui, C. Watanabe, K. Nakade, Y. Saiwai, T. Katsuragawa, M. Tsujimoto, R. Yoshizaki, T. Yamamoto, H. Minami, R. A. Klemm and K. Kadowaki, Appl. Phys. Lett. **107**, 82601 (2015).

IntechOpen